Chinese Journal of Aeronautics, (2020), xxx(xx): xxx–xxx

Chinese Society of Aeronautics and Astronautics
& Beihang University

Chinese Journal of Aeronautics

cja@buaa.edu.cn
www.sciencedirect.com

Advanced high-order nonlinear chirp scaling algorithm for high-resolution wide-swath spaceborne SAR

Zhirong MEN [a], **Pengbo WANG** [a,*], **Jie CHEN** [a], **Chunsheng LI** [a], **Wei LIU** [b], **Wei YANG** [a]

[a] *School of Electronic and Information Engineering, Beihang University, Beijing 100083, China*
[b] *Electronic and Electronic Engineering Department, University of Sheffield, Sheffield S1 3JD, UK*

Received 23 March 2020; revised 14 May 2020; accepted 11 July 2020

KEYWORDS

High-Resolution Wide-Swath (HRWS);
Imaging method;
Second-Order Equivalent Squint Range Model (SOESRM);
Signal processing;
Synthetic Aperture Radar (SAR)

Abstract Spaceborne Synthetic Aperture Radar (SAR) is a well-established and powerful imaging technology that can provide high-resolution images of the Earth's surface on a global scale. For future SAR systems, one of the key capabilities is to acquire images with both high-resolution and wide-swath. In parallel to the evolution of SAR sensors, more precise range models, and effective imaging algorithms are required. Due to the significant azimuth-variance of the echo signal in High-Resolution Wide-Swath (HRWS) SAR, two challenges have been faced in conventional imaging algorithms. The first challenge is constructing a precise range model of the whole scene and the second one is to develop an effective imaging algorithm since existing ones fail to process high-resolution and wide azimuth swath SAR data effectively. In this paper, an Advanced High-order Nonlinear Chirp Scaling (A-HNLCS) algorithm for HRWS SAR is proposed. First, a novel Second-Order Equivalent Squint Range Model (SOESRM) is developed to describe the range history of the whole scene, by introducing a quadratic curve to fit the deviation of the azimuth FM rate. Second, a corresponding algorithm is derived, where the azimuth-variance of the echo signal is solved by azimuth equalizing processing and accurate focusing is achieved through a high-order nonlinear chirp scaling algorithm. As a result, the whole scene can be accurately focused through one single imaging processing. Simulations are provided to validate the proposed range model and imaging algorithm.

* Corresponding author.
E-mail address: wangpb7966@buaa.edu.cn (P. WANG).
Peer review under responsibility of Editorial Committee of CJA.

Production and hosting by Elsevier

1. Introduction

Spaceborne Synthetic Aperture Radar (SAR) is a well-established remote sensing technology, capable of acquiring images of Earth's surface independent of weather conditions and sunlight illumination. With beam steering techniques,

https://doi.org/10.1016/j.cja.2020.08.035
1000-9361 © 2020 Chinese Society of Aeronautics and Astronautics. Production and hosting by Elsevier Ltd.

Please cite this article in press as: MEN Z et al. Advanced high-order nonlinear chirp scaling algorithm for high-resolution wide-swath spaceborne SAR, *Chin J Aeronaut* (2020), https://doi.org/10.1016/j.cja.2020.08.035

the sliding spotlight mode has been employed to support high-resolution applications. Since the first spaceborne SAR, Seasat was launched in 1978,[1,2] significant progress has been made in this area. With the launch of the SAR satellites Radarsat-2, TerraSAR-X, TanDEM-X, COSMO SkyMed, ALOS-2 and COSMO SkyMed Second Generation (CSG), the resolution of spaceborne SAR has been upgraded from tens of meters to the sub-meter level, and the ratio of imaging area to resolution element has been increased from 50 million to 252 million.[2–9] Benefiting from an advanced SAR sensor technology, the TerraSAR-X Next Generation (TSX-NG) will allow a high spatial resolution down to 0.25 m and a 5 km swath in both azimuth and range directions.[10,11] For TSX-NG, the ratio of imaging area to resolution element will increase to 400 million. In the future, spaceborne SAR systems are expected to acquire much wider areas with high-resolution for numerous applications. Suppose the swath of High-Resolution Wide-Swath (HRWS) SAR can be enlarged to 20 km (Azimuth) × 20 km (Range) with the same resolution of TSX-NG, the ratio of image area to resolution element would reach 6.4 billion, much higher than the magnitude of current SAR systems. Studies have demonstrated that through a longer integration time, a larger squint angle and adopting the Continuously Varying Pulse Repetition Frequency (CVPRF) strategy, the echo signal can be effectively acquired.[12] However, the much longer integration time and larger squint angle in azimuth would pose many challenges for spaceborne SAR signal processing, particularly the imaging part.

Among them is how to construct a precise range model to describe the range history more accurately in the HRWS case. Many studies have been performed in this area, with various accurate range models put forward. The most well-known range model in spaceborne SAR is the Hyperbolic Range Equation Model (HREM) or the Equivalent Squint Range Model (ESRM),[13,14] which is derived from the straight track and is adapted to the curved orbit of spaceborne SAR by equivalent velocity and squint angle. Based on either HREM or ESRM, several variations have been proposed and applied in the classic imaging algorithms. A Fourth-order Doppler Range Model (DRM4) was proposed for high-resolution spaceborne SAR, where the range model perfectly compensates the actual range history up to the quartic term.[15] An Advanced Hyperbolic Range Equation (AHRE) was introduced for Medium Earth Orbit (MEO) SAR, where an additional linear term is introduced into the conventional HREM to handle the focusing issue of an azimuth resolution around 3 m with altitude ranging from 1000 to 10000 km.[16] A Modified Equivalent Squint Range Model (MESRM) was developed for high-resolution spaceborne SAR, where an additional cubic component and quartic component are introduced into the conventional ESRM, and a better imaging result can be obtained.[17] Recently, range model for curvilinear trajectory airborne SAR, which involves three-dimensional velocity and acceleration is proposed. Based on Chebyshev approximation, the range model in the form of equivalent hyperbolic equation is obtained and shows high precise for a target point within its synthetic aperture time.[18]

However, all these studies are focused on the range model of a single point target, without considering the influence of azimuth-variance on the whole scene. As a result, the ground scenes in their simulations were both chosen as 4 km in azimuth by Luo[15] and Wang[17] et al, when the resolution is set between 0.25–0.30 m. Once the azimuth swath is enlarged to 20 km, the targets at the azimuth edge will suffer from severe degradation due to the mismatch between the range model and the Doppler parameter, which varies significantly along with different targets in the azimuth direction. To describe the azimuth-variance of the Doppler parameter, a Second-Order ESRM (SOESRM) is proposed in this paper, where a quadratic curve is introduced to fit the deviation of azimuth FM rate, so that a more accurate description of range history can be obtained.

Regarding the focusing algorithm for spaceborne SAR, the Chirp Scaling Algorithm (CSA) is commonly employed due to its good phase preservation and high-efficiency properties.[19] To improve the performance, some modified CSAs have been proposed, such as the Advanced Non-Linear Chirp Scaling (A-NLCS) algorithm,[16] the Higher-order Hybrid Correlation Algorithm (HHCA)[17] and the High-order NonLinear Chirp Scaling (HNLCS) algorithm.[20] However, all these algorithms are focused on compensating for the spatial variant cross-coupling phase between range and azimuth, without considering the azimuth-variance of the Doppler parameters. As a result, they cannot be applied to HRWS spaceborne SAR directly.

In this work, an Advanced High-order Nonlinear Chirp Scaling (A-HNLCS) algorithm is proposed, where the azimuth-variance of the Doppler parameters is removed by equalization filtering, and accurate focusing is realized through the higher-order nonlinear chirp scaling algorithm. The residual azimuth-variance, image aliasing, and geometric distortion are removed by a modified resampling process. Simulations are performed to show significantly improved imaging results.

It is necessary to point out that researchers of the German Aerospace Center (DLR) have also proposed a concept of HRWS mode which aims to achieve a high resolution (meter level) in azimuth direction and a wide swath (hundreds of kilometers) in range direction.[21,22] However, there are mainly two differences between the HRWS mode of DLR and the concept discussed in this paper. Firstly, DLR aims to operate in a 2 m azimuth resolution with a 400 km range swath using both Digital Beam-Forming (DBF) and multi-channel techniques to extend the capability of SAR systems,[21] but in this paper, we emphasize a much higher azimuth resolution (0.25 m) with 20 km swath in azimuth by increasing the squint angle of SAR. Secondly, challenges faced in signal processing for the two concepts are different. For the HRWS mode of DLR, the main challenge is the processing of the loss of pulses caused by blockage over a large range swath.[22] Meanwhile, due to the 2 m azimuth resolution, the ERSM and CSA are precise enough for signal processing. In this paper, azimuth variance becomes the main challenge for 0.25 m azimuth resolution and 20 km swath in both azimuth and range directions, hence, a more precise range model and a more effective imaging algorithm are required. Generally, the concept of DLR emphasizes the coverage to observe large-scope areas, but the concept in this paper focuses on the observation of high-value targets with a very high resolution and wide swath.

This paper is organized as follows: Based on azimuth-variance analysis of the range history, a second-order ERSM is proposed in Section 2. The corresponding advanced imaging algorithm for HRWS spaceborne SAR is developed in Sec-

Please cite this article in press as: MEN Z et al. Advanced high-order nonlinear chirp scaling algorithm for high-resolution wide-swath spaceborne SAR, *Chin J Aeronaut* (2020), https://doi.org/10.1016/j.cja.2020.08.035

tion 3. Simulation results are provided in Section 4, and conclusions are drawn in Section 5.

2. Modified range model

An accurate range model is the basis of SAR signal processing, which describes not only the range history of point targets but also the variation of Doppler parameters. The spaceborne SAR geometry in Earth-centered rotating coordinates is illustrated in Fig. 1, where the actual path is represented by the black solid line, and the paths based on HREM and MESRM are denoted by the blue dotted line and red dashed line, respectively. T_1 and T_3 represent the edge points of the scene in the azimuth direction, and T_2 presents the center point. S_i and E_i, where $i = \{1, 2, 3\}$, are the start and end positions of the illumination for the corresponding target T_i. It can be seen that MESRM can match the range history of T_2, but not precise enough for the points which are far away from the azimuth center, i.e., T_1 and T_3. R_0 is the slant range at Doppler center time of T_2.

By introducing an additional cubic component and quartic component into the conventional ESRM, MESRM is given as[20]

$$R(t, r_0) = \sqrt{r_0^2 + v_0^2 t^2 - 2 r_0 v_0 t \cos\varphi_0 + \Delta a_3 t^3 + \Delta a_4 t_4} \tag{1}$$

$$\begin{cases} v_0 = \sqrt{\left(\frac{\lambda f_d}{2}\right)^2 - \frac{\lambda r_0 f_r}{2}} \\ \varphi_0 = \arccos\frac{\lambda f_d}{2 v_0} \\ \Delta a_3 = \frac{-\lambda r_0 f_{r3}}{6} - \frac{v_0^3 \sin^2\varphi_0 \cos\varphi_0}{r_0} \\ \Delta a_4 = \frac{-\lambda r_0 f_{r4}}{24} + \frac{v_0^4 \sin^2\varphi_0}{4 r_0^2}(1 - 5\cos^2\varphi_0) - \frac{\Delta a_3 v_0 \cos\varphi_0}{r_0} \end{cases} \tag{2}$$

where t is the azimuth time, r_0 is the slant range at Doppler center time, v_0 is the equivalent radar velocity between the scatter and the SAR, φ_0 is the equivalent squint angle, Δa_3 and Δa_4 represent cubic and quartic coefficients, λ is the signal wavelength, and f_d, f_r, f_{r3} and f_{r4} denote the Doppler centroid frequency, the azimuth Frequency Modulation (FM) rate, the rate of the azimuth FM rate and the second-order derivative of the azimuth FM rate, respectively.

Differentiating Eq. (1) with respect to t for the point with a distance of x_0 from the scene center, we have

$$\frac{\partial R(t, r_0, x_0)}{\partial t} = -\frac{\lambda f_d(t, r_0, x_0)}{2} - \frac{\lambda f_r(t, r_0, x_0)}{2}(t - t_0) + \cdots \tag{3}$$

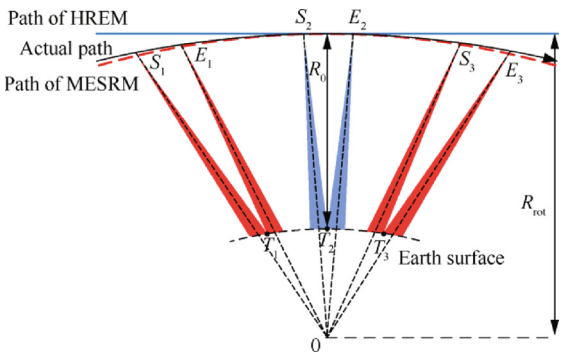

Fig. 1 Geometry of sliding spotlight mode for spaceborne SAR.

$$f_d(t, r_0, x_0) = -\frac{2v_0^2(t - t_0) - 2 r_0 v_0 \cos\varphi_0 + 3\Delta a_3 (t - t_0)^2 + 4\Delta a_4 (t - t_0)^3}{\lambda R(t, r_0, x_0)} \tag{4}$$

$$f_r(t, r_0, x_0) = -\frac{2v_0^2 + 6\Delta a_3 (t - t_0) + 12\Delta a_4 (t - t_0)^2}{\lambda R(t, r_0, x_0)} + \frac{\left[2v_0^2 (t - t_0) - 2 r_0 v_0 \cos\varphi_0 + 3\Delta a_3 (t - t_0)^2 + 4\Delta a_4 (t - t_0)^3\right]^2}{2\lambda R(t, r_0, x_0)^3} \tag{5}$$

where t_0 is the azimuth time when the target at x_0 is illuminated by the center of the radar beam.

From Eqs. (4) and (5), it can be seen that for MESRM there is a mapping relationship between $f_d(t, r_0, x_0)$ and $f_r(t, r_0, x_0)$, as shown in Fig. 2 (red line), and the simulation parameters are listed in Table 1. For the point with a distance of x_0 from the scene center, there is a $f_d(t, r_0, x_0)$ and a corresponding $f_r(t, r_0, x_0)$. Generally, if the Doppler parameters of all the targets match the mapping relationship of the actual situation (the blue dashed line in Fig. 2), precise focusing of the whole scene can be realized through one single imaging process. However, due to the earth rotation and curved orbit, there is an obvious deviation as targets move away from the scene center, as shown in the red box of Fig. 2. Moreover, the Doppler FM rate error as a function of azimuth position caused by MESRM is given in Fig. 3, where the red dashed lines are the safe lines corresponding to a maximal phase error of $\pi/4$. The result indicates that the edge targets would suffer from severe degradation and the effective imaging area is close to 4 km in azimuth when MESRM is implemented. The imaging result cannot meet the requirement of a larger scene, such as 20 km in azimuth. Therefore, a more precise range model is needed to solve the azimuth-variance phenomenon for HRWS SAR.

To describe the azimuth-variance of the Doppler parameters, a Second-Order ERSM (SOERSM) is proposed in this paper by introducing a quadric curve to fit the deviation of the azimuth FM rate. The azimuth FM rate and the rate of the azimuth FM rate can be expressed as follows:

$$\begin{cases} f_{r,\text{actual}}(t, r_0, x_0) = f_r(t, r_0, x_0) + \xi_1(r_0) t_0 + \frac{\xi_2(r_0)}{2} t_0^2 \\ f_{r3,\text{actual}}(t, r_0, x_0) = f_{r3}(t, r_0, x_0) + \xi_2(r_0) t_0 \end{cases} \tag{6}$$

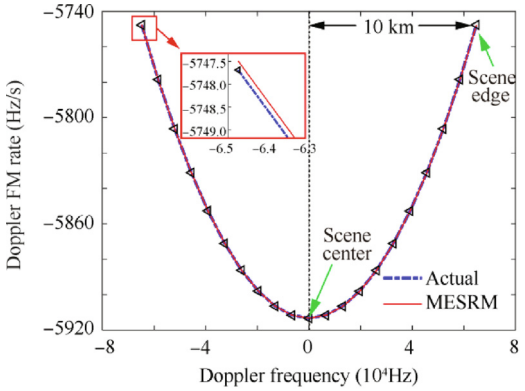

Note: that the distance between adjacent targets is 1 km, hence the length of the scene is 20 km in azimuth

Fig. 2 Mapping relationship between f_d and f_r for 21 point targets in azimuth.

Table 1 List of simulation parameters.

Description	Value
Height (km)	514
Eccentricity	0.0011
Inclination (°)	98
Longitude of ascending node (°)	0
Argument of perigee (°)	90
Carrier frequency (GHz)	9.6
Bandwidth (GHz)	1.2
Sampling frequency (GHz)	1.4
Look angle (°)	30
Antenna length (m)	4.8
Azimuth resolution (m)	0.25
Hybrid factor	0.10417

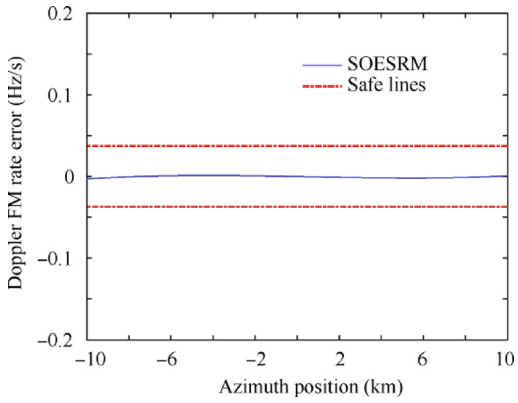

Fig. 4 Error of Doppler FM rate for different azimuth positions using SOERSM.

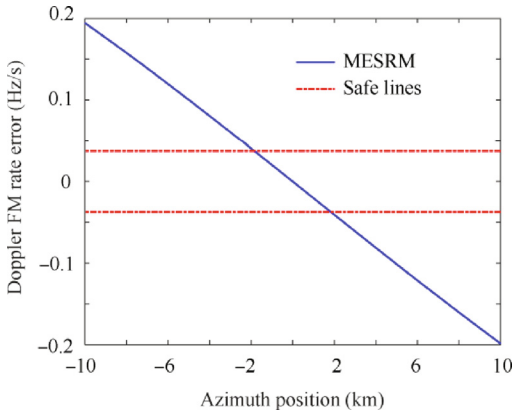

Fig. 3 Doppler FM rate error as a function of azimuth position caused by MESRM.

where $f_{r,\text{actual}}$ and $f_{r3,\text{actual}}$ represent the actual value of the azimuth FM rate and the rate of the azimuth FM rate; $\xi_1(r_0)$ and $\xi_2(r_0)$ are the first and second-order fitting coefficients.

Substituting Eq. (6) into Eq. (1), the range model can be modified as SOERSM

$$R(t,r_0,x_0) = \sqrt{r_0^2 - 2r_0v_0\Delta t\cos\varphi_0 + \Delta a_2'\Delta t^2 + \Delta a_3'\Delta t^3 + \Delta a_4\Delta t^4} \tag{7}$$

$$\begin{cases} \Delta a_2' = v_0^2 - \frac{\lambda r_0}{2}\left(\xi_1(r_0)t_0 + \frac{\xi_2(r_0)}{2}t_0^2\right) \\ \Delta a_3' = \Delta a_3 - \frac{\lambda r_0\xi_2(r_0)}{6}t_0 \end{cases} \tag{8}$$

where $\Delta t = t - t_0$.

With SOERSM, the error of $f_r(t,r_0,x_0)$ caused by targets moving away from the scene center, is compensated effectively. Fig. 4 shows the Doppler FM rate error, where it can be seen that the error of the Doppler FM rate is limited within the safe lines and the effective imaging swath can be enlarged to 20 km in azimuth. Hence, SOERSM is more suitable for HRWS SAR.

Orbit error (velocity error and position error of SAR satellite) would introduce error to the estimates of parameters of range models such as Doppler frequency, Doppler FM frequency, etc. Also, this is a challenge for all range models and SAR systems are equipped to offer accurate orbit measurements. The absolute 3-D orbit accuracy of TerraSAR-X is better than 10 cm,[23] and the 3-D orbit and velocity accuracy of Gaofen-3 is better than 5 cm and 0.05 mm/s,[24] respectively. Analysis of Doppler FM rate error caused by SOESRM and MESRM with velocity error fixed as 0.05 mm/s and position error fixed as 10 cm is given in Fig. 5. It can be seen that the error of the Doppler FM rate is still within the safe lines based on current orbit and velocity accuracy, which means that well-focused images can be achieved by the range model of SOESRM.

To compare the difference between MESRM and the proposed SOERSM, we expand the range model of Eq. (7) based on Taylor polynomial as Eq. (9) (see Appendix A). Also, Chebyshev orthogonal decomposition is another strategy for the expansion of the range model.[18]

$$R(t,r_0,x_0) \approx R_1(t,r_0,x_0) + R_2(t,r_0,x_0) + R_3(t,r_0,x_0) \tag{9}$$

where

$$\begin{cases} R_1(t,r_0,x_0) = \sqrt{r_0^2 - 2r_0v_0\Delta t\cos\varphi_0 + v_0^2\Delta t^2 + \left(\Delta a_3 + \frac{\lambda r_0\xi_1(r_0)}{6}\right)\Delta t^3 + \left(\Delta a_4 + \frac{\lambda r_0\xi_2(r_0)}{24}\right)\Delta t^4} \\ R_2(t,r_0,x_0) = -\frac{\lambda\xi_1(r_0)}{12}t^3 - \frac{\lambda\xi_2(r_0)}{48}t^4 \\ R_3(t,r_0,x_0) = \left(\frac{\lambda\xi_1(r_0)r_0^2}{4} + \frac{\lambda\xi_2(r_0)r_0^3}{12}\right)\Delta t + \frac{\lambda\xi_1(r_0)r_0^3}{12} + \frac{\lambda\xi_2(r_0)r_0^4}{48} \end{cases} \tag{10}$$

According to Eqs. (7) and (10), a few remarks would facilitate a better understanding of the characteristics of SOERSM.

(1) The first part $R_1(t,r_0,x_0)$ is similar to MESRM, which is azimuth-invariant and can be compensated using the traditional high-resolution imaging algorithm.

(2) The second part $R_2(t,r_0,x_0)$ consists of a cubic term and a quartic term, which is the same for all targets and can be compensated before focusing.

(3) The last part $R_3(t,r_0,x_0)$ is made up of a linear term and a constant term, which is azimuth-variant. The constant term causes a range shift $\Delta r_1(r_0,x_0)$ and also brings in a phase error $\Delta\varphi_1(r_0,x_0)$, while the linear term leads to a Doppler centroid error, which not only introduces a phase error $\Delta\varphi_2(r_0,x_0)$, but also causes a range shift $\Delta r_2(r_0,x_0)$ and an azimuth shift $\Delta x_2(r_0,x_0)$. Considering the azimuth-variant property, these terms should be compensated after focusing. The items of the errors above are given in Eqs. (11) and (12).

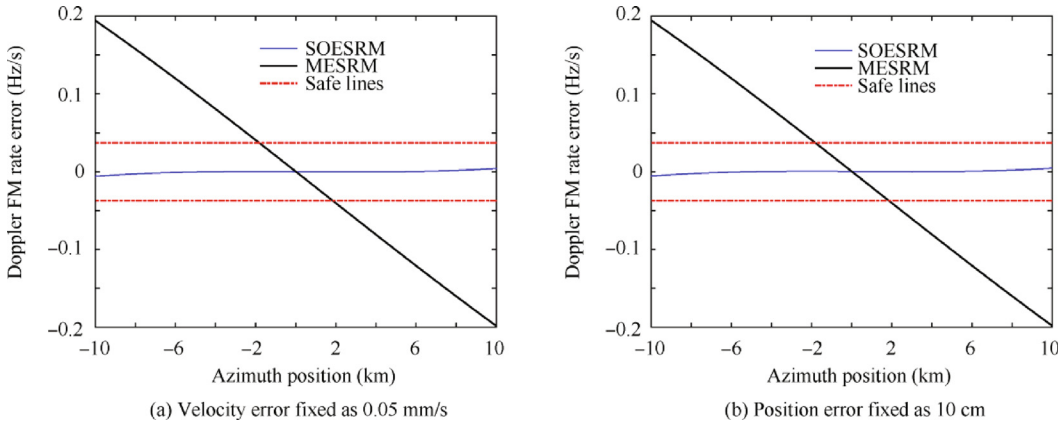

Fig. 5 Doppler FM rate error caused by SOESRM and MESRM with velocity error fixed as 0.05 mm/s or position error fixed as 10 cm of satellite.

$$\begin{cases} \Delta\varphi_1(r_0,x_0) = -\frac{\pi\xi_1(r_0)}{3}t_0^3 - \frac{\pi\xi_2(r_0)}{12}t_0^4 \\ \Delta\varphi_2(r_0,x_0) = -\pi\frac{\Delta f_d^2(r_0,x_0)}{f_r(r_0,x_0)} \end{cases} \tag{11}$$

$$\begin{cases} \Delta r_1(r_0,x_0) = \frac{\lambda\xi_1(r_0)}{12}t_0^3 + \frac{\lambda\xi_2(r_0)}{48}t_0^4 \\ \Delta r_2(r_0,x_0) = -\frac{\lambda f_d(r_0,x_0)\Delta f_d(r_0,x_0)}{2f_r(r_0,x_0)} - \frac{\lambda\Delta f_d^2(r_0,x_0)}{4f_r(r_0,x_0)} \\ \Delta x_2(r_0,x_0) = \frac{\Delta f_d(r_0,x_0)}{f_r(r_0,x_0)}v_g \end{cases} \tag{12}$$

where $\Delta f_d(r_0,x_0) = -\frac{\xi_1(r_0)}{2}t_0^2 - \frac{\xi_2(r_0)}{6}t_0^3$ and v_g is the ground velocity.

In general, the premise of the expansion in Eq. (9) is to guarantee the phase error is within $\pi/4$. Hence, it is necessary to analyse the feasibility of the expansion. To show the accuracy of the expansion of SOERSM, the phase error as a function of illumination time is given in Fig. 6, using the orbit and radar parameters listed in Table 1. Lines with different colours represent the phase error of different targets in azimuth. There are 21 targets and the distance between adjacent points is 1 km. It can be seen that the maximum value of phase error is still within $\pi/4$, which means that the expansion is effective and would not cause severe degradation to signal processing.

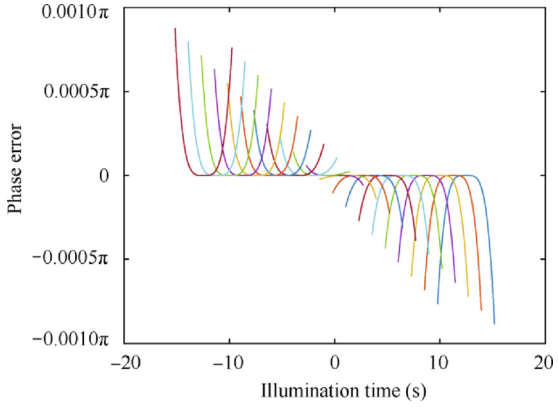

Fig. 6 Phase error as a function of illumination time caused by approximation of SOESRM.

3. Proposed imaging algorithm

Based on the aforementioned discussion, an advanced nonlinear chirp scaling algorithm is proposed here. The block diagram of the proposed algorithm is shown in Fig. 7. There are three parts: the first part is azimuth preprocessing, which is used to avoid azimuth aliasing and remove the azimuth-variance caused by $R_2(t,r_0,x_0)$; the second part is high-precision focusing within the full swath; the last part is residual phase compensation, which is used to remove image aliasing, residual azimuth-variance and realize geometric correction caused by $R_3(t,r_0,x_0)$. In the following, details of the basic operations are provided according to the signal flow in the diagram.

3.1. Azimuth preprocessing

To remove the azimuth-variance of the Doppler parameter and azimuth aliasing of the Doppler spectrum, an improved azimuth sub-aperture processing is performed firstly. Compared with the traditional one,[15] an equalizing filter is introduced to remove the azimuth-variance, and the equalizing filter function $H_1(f_\tau,t)$ is given by

$$\begin{aligned} H_1(f_\tau,t) = \exp\left(-\mathrm{j}\frac{\pi\xi_1(r_{\mathrm{ref}})}{3}(t_k+t)^3 - \mathrm{j}\frac{\pi\xi_2(r_{\mathrm{ref}})}{12}(t_k+t)^4\right) \\ \cdot\exp\left(-\mathrm{j}2\pi\left\lfloor\left(1+\frac{f_\tau}{f_c}\right)f_{\mathrm{d},k}T_{\mathrm{sub}}\right\rfloor\frac{f_{\mathrm{prf}}}{N_{\mathrm{sub}}}\mathrm{t}\right) \end{aligned} \tag{13}$$

where the first exponential term is used to remove the azimuth-variance of the echo signal, and the second one is used to reduce the effect of the transmitted bandwidth; r_{ref} denotes the reference slant range; f_{prf} represents the Pulse Repetition Frequency (PRF); f_c represents the carrier frequency; N_{sub} is the azimuth sample number of the sub-aperture; T_{sub} is the size of the sub-aperture; $f_{\mathrm{d},k}$ is the Doppler centroid frequency of the kth sub-aperture; t_k is the center time of the kth sub-aperture, and $\lfloor\cdot\rfloor$ is the rounding operation.

After azimuth equalizing filter processing, sub-aperture azimuth FFT, delay phase compensation and sub-aperture recombination are performed for azimuth sub-aperture processing, and the 2-D signal spectrum data are obtained in a discrete form without aliasing in the azimuth direction. The delay phase function $H_2(f_\tau,k)$ can be expressed as follows:

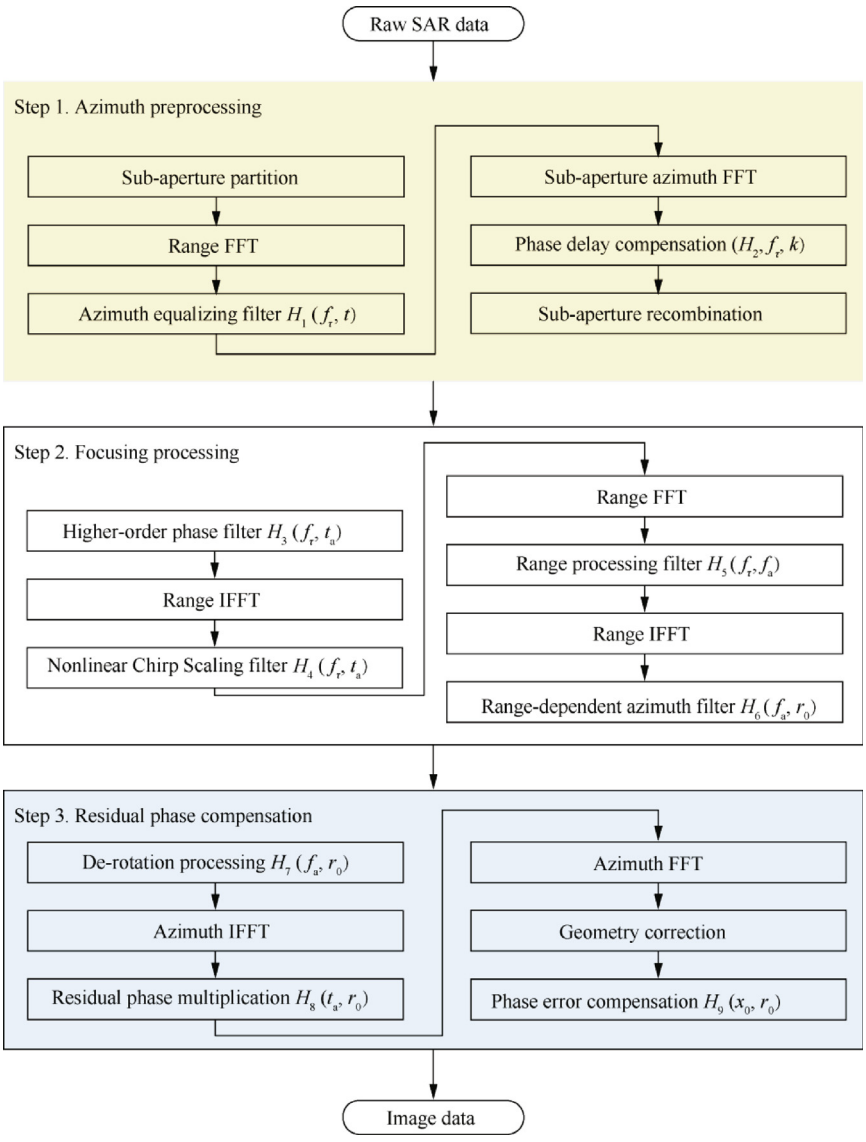

Fig. 7 Block diagram of proposed advanced high-order nonlinear chirp scaling algorithm.

$$H_2(f_\tau, k) = \exp\left(-\mathrm{j}2\pi\left[\left(1+\frac{f_\tau}{f_c}\right)f_{\mathrm{d},k}T_{\mathrm{sub}}\right]\frac{f_{\mathrm{prf}}}{N_{\mathrm{sub}}}t_k\right) \tag{14}$$

Based on the proposed range model, after demodulation to baseband, the received signal for the point target at x_0 can be described as

$$S(\tau, t, r_0, x_0) = \sigma_0\omega_{\mathrm{r}}\left(\tau - \frac{2R(t, r_0, x_0)}{c}\right)\exp\left(-\frac{\mathrm{j}4\pi R(t, r_0, x_0)}{\lambda}\right) \cdot \omega_{\mathrm{a}}(t - t_0)\exp\left(-\mathrm{j}\pi K_{\mathrm{r}}\left(\tau - \frac{2R(t, r_0, x_0)}{c}\right)^2\right) \tag{15}$$

where σ_0 represents the scattering coefficient, t_0 is the Doppler center time, τ represents the fast time, c is the speed of light, K_{r} is the range chirp rate, $\omega_{\mathrm{r}}(\cdot)$ and $\omega_{\mathrm{a}}(\cdot)$ denote antenna pattern functions in the range and azimuth directions, respectively. x_0 is the azimuth position of the target.

Using the principle of stationary phase and Fourier transformation, the 2-D Point Target Spectrum (PTS) of Eq. (15) can be obtained as (see Appendix B)

$$S(f_{\mathrm{a}}, f_\tau, r_0, x_0) = \sigma_0 W_{\mathrm{r}}(f_\tau) W_{\mathrm{a}}(f_{\mathrm{a}})\exp(\Phi_{\mathrm{azi}}(f_{\mathrm{a}}, r_0, x_0))\exp(\Phi_{\mathrm{HOP}}(f_{\mathrm{a}}, f_\tau, r_0, x_0)) \cdot\exp(\Phi_{\mathrm{RCM}}(f_{\mathrm{a}}, f_\tau, r_0, x_0))\exp(\Phi_{\mathrm{rg2}}(f_{\mathrm{a}}, f_\tau, r_0, x_0)) \cdot\exp\left(-\mathrm{j}\pi\frac{4\xi_1(r_{\mathrm{ref}})r_0^3 + \xi_2(r_{\mathrm{ref}})r_0^4}{12}\right)\exp\left(\mathrm{j}\pi\frac{(f_{\mathrm{a}} - f'_{\mathrm{d}})^2\Delta\xi_1(r_0)t_0}{f_\tau^2}\right) \tag{16}$$

where

$$\Phi_{\mathrm{azi}}(f_{\mathrm{a}}, r_0, x_0) = -\mathrm{j}\frac{4\pi}{\lambda}\left[r'_0 - \frac{\lambda^2(f_{\mathrm{a}} - f'_{\mathrm{d}})^2}{8}\alpha(r_0) + \frac{\lambda^3(f_{\mathrm{a}} - f'_{\mathrm{d}})^3}{24}\beta(r_0) - \frac{\lambda^4(f_{\mathrm{a}} - f'_{\mathrm{d}})^4}{64}\gamma(r_0)\right] \tag{17}$$

$$\Phi_{\mathrm{RCM}}(f_\tau, f_{\mathrm{a}}, r_0, x_0) = -\mathrm{j}\frac{\pi}{c}\left[4r'_0 + \frac{\lambda^2(f_{\mathrm{a}}^2 - f_{\mathrm{d}}^2)}{2}\alpha(r_0) - \frac{\lambda^3(2f_{\mathrm{a}} + f'_{\mathrm{d}})(f_{\mathrm{a}} - f'_{\mathrm{d}})^2}{6}\beta(r_0)\right]f_\tau - \mathrm{j}\frac{\pi\lambda^4(3f_{\mathrm{a}} + f'_{\mathrm{d}})(f_{\mathrm{a}} - f'_{\mathrm{d}})^3}{64c}\gamma(r_0)f_\tau \tag{18}$$

$$\Phi_{rg2}(f_\tau,f_a,r_0,x_0)=-j\frac{\pi f_\tau^2}{K_r}+j\frac{\pi\lambda f_a^2}{2f_c^2}\left[\alpha(r_0)-\lambda(f_a-f_d')\beta(r_0)+\frac{3\lambda^2(f_a-f_d')^2}{4}\gamma(r_0)\right]f_\tau^2 \quad (19)$$

$$\begin{aligned}\Phi_{HOP}(f_\tau,f_a,r_0,x_0)=&-j2\pi f_a t_a(f_\tau,f_a,r_0,x_0)-j4\pi\left(\tfrac{1}{\lambda}+\tfrac{f_\tau}{c}\right)R(t_a(f_\tau,f_a,r_0,x_0))\\&-\Phi_{azi}(f_a,r_0,x_0)-\Phi_{RCM}(f_a,f_\tau,r_0,x_0)-\Phi_{rg2}(f_a,f_\tau,r_0,x_0)\end{aligned} \quad (20)$$

where $t_a(\cdot)$ is the stationary point, $r_0'=r_0+\frac{\lambda\xi_1(r_0)}{12}t_0^3+\frac{\lambda\xi_2(r_0)}{48}t_0^4$, $f_d'(r_0,x_0)=f_d(r_0,0)+\Delta f_d(r_0,x_0)$, $\Delta\xi_1(r_0)=\xi_1(r_0)-\xi_1(r_{ref})$. f_d',f_d,f_r,f_{r3} and f_{r4} represent $f_d'(r_0,x_0)$,$f_d(r_0,0)$,$f_r(r_0,0)$,$f_{r3}(r_0,0)$ and $f_{r4}(r_0,0)$, respectively. α,β and γ are the Doppler parameters of the echo signal and can be calculated as $\alpha=\frac{-2}{\lambda f_r(r_0)}$, $\beta=\frac{-2f_{r3}(r_0)}{\lambda^2 f_r^3(r_0)}$ and $\gamma=\frac{4f_r(r_0)f_{r4}(r_0)-12f_{r3}(r_0)}{3\lambda^3 f_r^5(r_0)}$.

Considering the range-dependence of the Doppler parameters, a linear hypothesis is used to deduce the following imaging algorithm, as follows

$$\begin{cases}\alpha=\alpha_1+\alpha_2(r_0-r_{ref})\\ \beta=\beta_1+\beta_2(r_0-r_{ref})\\ \gamma=\gamma_1+\gamma_2(r_0-r_{ref})\end{cases} \quad (21)$$

where r_{ref} is the reference slant range. The corresponding parameters are v_{ref}, φ_{ref}, $\Delta a_{3,ref}$ and $\Delta a_{4,ref}$.

Substituting Eq. (21) into Eq. (16), the 2-D signal spectrum can be obtained, and the corresponding imaging algorithm is provided in the following section.

3.2. Focusing processing

Since the aliasing effect in the azimuth frequency domain is removed after the improved azimuth sub-aperture processing, the improved higher-order nonlinear chirp scaling algorithm can be employed to implement Range Cell Migration Correction (RCMC), range compression, Second Range Compression (SRC), as well as azimuth compression.

The algorithm starts with higher-order phase compensation and cubic phase filtering in the 2-D frequency domain, as follows

$$H_3(f_\tau,f_a)=\exp(-\Phi_{HOP}(f_\tau,f_a,r_{ref}))\cdot\exp\left(j\frac{2\pi}{3}Y(f_a)f_\tau^3\right) \quad (22)$$

where the first exponential term is used to remove the higher-order cross-coupling, and the second exponential term is introduced to provide an accurate accommodation of range dependence of SRC. $Y(f_a)$ is the azimuth-frequency varying cubic phase filter coefficient, given by

$$Y(f_a)=-\frac{\lambda f_a^2\left[4\alpha_2-4\lambda(f_a-f_d)\beta_2+3\lambda^2(f_a-f_d)^2\gamma_2\right]}{8f_c^2K_m(f_a,r_{ref})(c\tau_2^2(f_a)+2\tau_2(f_a))} \quad (23)$$

where

$$\begin{aligned}\tfrac{1}{K_m(f_a,r_0)}=&-\tfrac{1}{K_r}-\tfrac{\lambda f_a^2}{2f_c^2}\left[\alpha_1-\lambda(f_a-f_d)\beta_1+\tfrac{3}{4}\lambda^2(f_a-f_d)^2\gamma_1\right]\\&-\tfrac{\lambda f_a^2}{2f_c^2}\left[\alpha_2-\lambda(f_a-f_d)\beta_2+\tfrac{3}{4}\lambda^2(f_a-f_d)^2\gamma_2\right](r_0-r_{ref})\end{aligned} \quad (24)$$

$$\tau_2(f_a)=\frac{\lambda^2(f_a^2-f_d^2)}{4c}\alpha_2-\frac{\lambda^3(2f_a+f_d)(f_a-f_d)^2}{12c}\beta_2+\frac{\lambda^4(3f_a+f_d)(f_a-f_d)^3}{32c}\gamma_2 \quad (25)$$

After higher-order phase compensation and cubic phase filtering, the signal is transformed to the range-Doppler domain by range Inverse FFT (IFFT). Nonlinear chirp scaling processing is performed to remove the range dependence of SRC and RCM, where the nonlinear chirp scaling function $H_4(\tau,f_a)$, centered at the reference range $\tau_d(f_a,r_{ref})$, is given by

$$\begin{aligned}H_4(\tau,f_a)=&\exp\left(-j\frac{2\pi}{3}q_3(f_a)(\tau-\tau_d(f_a,r_{ref}))^3\right)\\&\cdot\exp\left(-j\pi q_2(f_a)(\tau-\tau_d(f_a,r_{ref}))^2\right)\end{aligned} \quad (26)$$

where $q_2(f_a)$ and $q_3(f_a)$ denote the quadratic and cubic coefficients

$$\begin{cases}q_2(f_a)=-\frac{c}{2}K_m(f_a,r_{ref})\tau_2(f_a)\\ q_3(f_a)=\frac{c^2}{4}Y(f_a)K_m^3(f_a,r_{ref})\tau_2^2(f_a)\end{cases} \quad (27)$$

$$\tau_d(f_a,r_0)=\frac{2r_0}{c}+\tau_1(f_a)+\tau_1(f_a)(r_0-r_{ref}) \quad (28)$$

$$\tau_1(f_a)=\frac{\lambda^2(f_a^2-f_d^2)}{4c}\alpha_1-\frac{\lambda^3(2f_a+f_d)(f_a-f_d)^2}{12c}\beta_1+\frac{\lambda^4(3f_a+f_d)(f_a-f_d)^3}{32c}\gamma_1 \quad (29)$$

After nonlinear chirp scaling processing, the signal can be expressed as

$$\begin{aligned}S(\tau,f_a,r_0,x_0)=&\sigma_0 w_r(\tau)W_a(f_a)\\&\cdot\exp\left(-j\frac{2\pi}{3}Y(f_a)K_m^3(f_a,r_{ref})(1-\tau_2^2(f_a))\Delta\tau^3\right)\\&\cdot\exp(\Phi_0(f_a,r_0,x_0))\exp(\Phi_{azi}(f_a,r_0,x_0))\\&\cdot\exp\left(j\pi K_m(f_a,r_{ref})\left(1+\frac{c}{2}\tau_2(f_a)\right)\Delta\tau^2\right)\\&\cdot\exp\left(-j\pi\frac{4\xi_1(r_{ref})t_0^3+\xi_2(r_{ref})t_0^4}{12}\right)\\&\cdot\exp\left(j\pi\frac{(f_a-f_d')^2\Delta\xi_1(r_0)t_0}{f_r^2}\right)\end{aligned} \quad (30)$$

where

$$\begin{aligned}\Phi_0(f_a,r_0,x_0)=&\left(j\pi K_m(f_a,r_0)\tau_2^2(f_a)-j4\pi\frac{q_2}{c^2}\right)(r_0-r_{ref})^2\\&-\left(j\frac{2\pi}{3}Y(f_a)K_m^3(f_a,r_0)\tau_2^3(f_a)-j\frac{16\pi q_3}{3c^3}\right)(r_0-r_{ref})^3\end{aligned} \quad (31)$$

$$\Delta\tau=\tau-\frac{2r_0'}{c}-\tau_1(f_a) \quad (32)$$

From Eq. (30), it can be seen that the RCMC and SRC are independent of range r_0, and the bulk RCMC and SRC can be performed accurately and effectively across the range swath. Accordingly, the range processing filter $H_5(f_\tau,f_a)$ is given by

$$\begin{aligned}H_5(f_\tau,f_a)=&\exp(j2\pi f_\tau\tau_1(f_a))\\&\cdot\exp\left(j\pi\frac{f_\tau^2}{K_m(f_a,r_{ref})\left(1+\frac{\tau_2(f_a)c}{2}\right)}\right)\\&\cdot\exp\left(-j\pi\frac{2Y(f_a)\left(1-\frac{\tau_2^2(f_a)c^2}{4}\right)f_\tau^3}{3\left(1+\frac{\tau_2(f_a)c}{2}\right)^3}\right)\end{aligned} \quad (33)$$

With range IFFT, the data is transformed back to the range-Doppler domain, and then range-dependent azimuth-matched filtering and residual phase compensation can be performed by the azimuth processing filter $H_6(f_a, r_0)$

$$H_6(f_a, r_0) = \exp(-\Phi_{azi}(f_a, r_0))\exp(-\Phi_0(f_a, r_0)) \tag{34}$$

3.3. Residual phase compensation

Since the target is focused by the higher-order nonlinear chirp scaling algorithm, image aliasing, residual azimuth-variance and realize geometric correction still exist. An azimuth resampling operation is applied to remove the existing residual phase.

The operation begins with de-rotation processing, and the de-rotation phase function $H_7(f_a, r_0)$ is given by

$$H_7(f_a, r_0) = \exp\left(-j\pi\frac{f_a^2}{f_{r,D}}\right)\exp\left(-j\pi\frac{\Delta\xi_1(r_0)f_a^3}{6f_r^3}\right) \tag{35}$$

where $\Delta\xi_1(r_0) = \xi_1(r_0) - \xi_1(r_{ref})$, $f_{r,D} = f_{r,rot}/H_f$, H_f denotes the hybrid factor, and $f_{r,rot}$ is the slope of the varying Doppler centroid introduced by beam steering, f_r denotes $f_r(r_0, 0)$.

After the azimuth IFFT, residual phase multiplication is performed to compensate the residual quadric and cubic phase. The residual phase function is given by

$$H_8(t, r_0) = \exp(-j\pi f_{r,D}t^2)\exp\left(j\pi\frac{\Delta\xi_1(r_0)f_{r,D}^3}{6f_r^3}t^3\right) \tag{36}$$

Then, the focused image can be obtained by azimuth FFT, which can be expressed in the following

$$\begin{aligned} S(\tau, t, r_0, x_0) = {} & A_r\left(\tau - \tfrac{2}{c}\left(r_0' - \tfrac{\lambda f_d \Delta f_d}{2f_r} - \tfrac{\lambda\Delta f_d^2}{4f_r}\right)\right) \\ & \cdot A_a\left(t_0 + \tfrac{\Delta f_d}{f_r} - \tfrac{\Delta\xi_1(r_0)f_d^2}{4f_r^3}\right)\exp\left(-j\pi\tfrac{\Delta f_d^2}{f_r}\right) \\ & \cdot\exp\left(-j\tfrac{4\pi r_0}{\lambda} - j\tfrac{\pi\xi_2(r_0)}{12}t_0^4 - j\tfrac{\pi\xi_1(r_0)}{3}t_0^3 - j\tfrac{\pi\Delta\xi_1(r_0)f_d^3}{6f_r^3}\right) \end{aligned} \tag{37}$$

From Eq. (37), we can see that there is geometric distortion and phase error in the focused image, and residual phase compensation and geometry correction are needed to obtain the accurately focused image. Here, we use Lagrange interpolation to realize geometry correction, and the mapping relationship is described in Eq. (38). The phase error is compensated by multiplying $H_9(x_0, r_0)$ with each pixel in the focused image.

$$\begin{cases} r_{r,0} = r_0' - \frac{\lambda f_d \Delta f_d}{2f_r} - \frac{\lambda\Delta f_d^2}{4f_r} \\ x_{r,0} = x_0 + \frac{\Delta f_d}{f_r}v_g - \frac{\Delta\xi_1 f_d^2}{4f_r^3}v_g \end{cases} \tag{38}$$

$$H_9(x_0, r_0) = \exp\left(j\pi\frac{\Delta f_d^2}{f_r} + j\pi\frac{\xi_2(r_0)}{12}t_0^4 + j\pi\frac{\xi_1(r_0)}{3}t_0^3 + j\pi\frac{\Delta\xi_1(r_0)}{6f_r^3}f_d^3\right) \tag{39}$$

4. Simulations and analysis

To demonstrate the performance of the proposed imaging algorithm, raw data is first generated for point targets using the parameters given in Table 1 and the scene shown in Fig. 8. The distances of different targets along the range and azimuth directions are 10.0 km and 1.0 km, respectively. Rectangular weighting is used for both azimuth and range processing. For SAR signal processing, range model is the foundation of an imaging algorithm. In Ref. [20], the accuracy of ESRM, DRM4, and MESRM has been compared (see Figs. 4 and 5 in Ref. [20]), and also focused results using NCS, ωkA and HHCA indicate that HHCA can achieve the best imaging quality when processing SAR data with a high resolution of 0.25 m (see Figs. 13 to 15 in Ref. [20]). Hence, HHCA is employed for the comparison with the proposed A-HNLCS algorithm.

Fig. 9 shows the Impulse Response Width (IRW) (normalized to the theoretical) curve to azimuth displacement, and Fig. 10 shows the Peak Sidelobe Ratio (PSLR) results to azimuth displacement. In the HHCA, the imaging performance degrades with azimuth displacement. Only targets near the scene center can be focused accurately, and the targets at the azimuth edge suffer from severe degradation. In the proposed A-HNLCS algorithm, all targets of the whole scene can be focused well. The deterioration of the IRW and PSLR is less than 0.5% and 3 %, respectively.

To quantify the focusing performance, the point target analysis results are listed in Table 2, where the ideal PSLR is −13.26 dB, using the rectangular window. The theoretical resolution is calculated according to the following equation:

$$\rho_{a,c} = \frac{A_L}{2}\cdot\frac{H_f r_0 + r_{ref} - r_0}{r_{ref}} \tag{40}$$

Fig. 11 shows the azimuth profile of PT1 and PT63, where the red dashed line represents the focused results by HHCA, and the blue solid line represents the focused results by the proposed A-HNLCS algorithm. It can be seen that the edge targets based on HHCA suffer from severe degradation, and significant azimuth main lobe broadening and sidelobe arising can be observed. Compared to the HHCA results, the focusing performance of the proposed algorithm has been improved significantly, and all of the targets are well focused by the proposed method. All these indicate that our proposed focusing algorithm can meet the imaging requirement of high-resolution wide-swath spaceborne SAR effectively.

Computational complexity of AHRE, A-NLCS, HHCA, and A-HNLCS is compared in Table 3. Times of both range

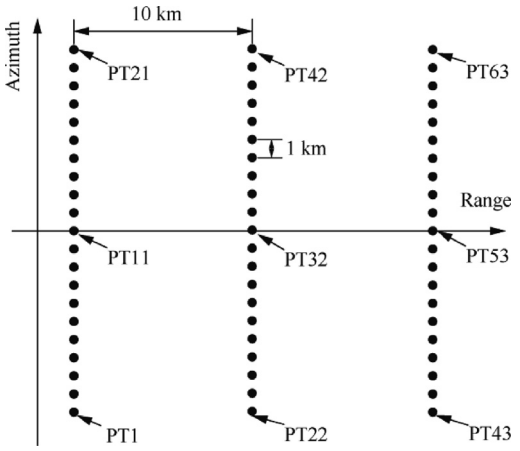

Fig. 8 Ground scene layout in our simulation.

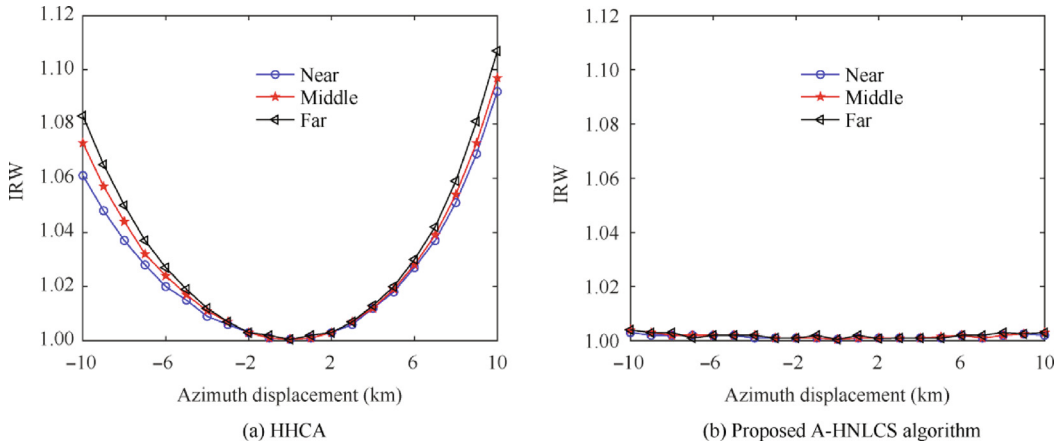

Fig. 9 IRW of the focused result.

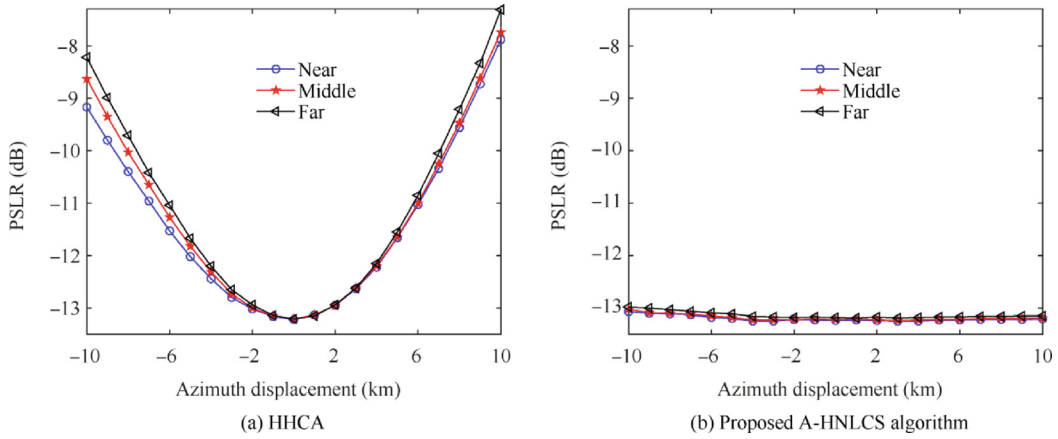

Fig. 10 PSLR of the focused result.

Table 2 Performance analysis of point targets.

Point target	HHCA			A-HNLCS algorithm		
	$\rho_{a,m}$ (m)	$\rho_{a,c}$ (m)	PSLR (dB)	$\rho_{a,m}$ (m)	$\rho_{a,c}$ (m)	PSLR (dB)
1	0.285	0.269	−9.17	0.270	0.269	−13.07
11	0.269	0.269	−13.22	0.269	0.269	−13.24
21	0.294	0.269	−7.88	0.270	0.269	−13.21
22	0.268	0.250	−8.63	0.251	0.250	−13.02
32	0.250	0.250	−13.21	0.250	0.250	−13.22
42	0.274	0.250	−7.74	0.251	0.250	−13.19
43	0.249	0.230	−8.22	0.231	0.230	−12.98
53	0.230	0.230	−13.21	0.230	0.230	−13.18
63	0.255	0.230	−7.31	0.231	0.230	−13.15

Fourier Transform (FT) and azimuth FT for the above algorithms are the same because they all based on CSA. The proposed A-HNLCS requires the most complex multiplication.

The computation can be described as[25]:

$$\frac{p}{2}N_aN_r\log_2(N_a)+\frac{q}{2}N_aN_r\log_2(N_r)+mN_aN_r \tag{41}$$

where p and q are the times of azimuth FT and range FT, respectively. m is the times of complex multiplication; N_a and N_r are the number of samples in azimuth and range directions.

The proportion of computation and total computational operations of four different algorithms are shown in Fig. 12 for a range of N_a and N_r. It indicates that FT always takes more than 80% of the computation for these four imaging algorithms, and the increasing complex multiplication of the proposed A-HNLCS would not cause much computation, as it is mainly dominated by FT. Furthermore, A-HNLCS can achieve the image of the whole scene instead of dividing the

Please cite this article in press as: MEN Z et al. Advanced high-order nonlinear chirp scaling algorithm for high-resolution wide-swath spaceborne SAR, *Chin J Aeronaut* (2020), https://doi.org/10.1016/j.cja.2020.08.035

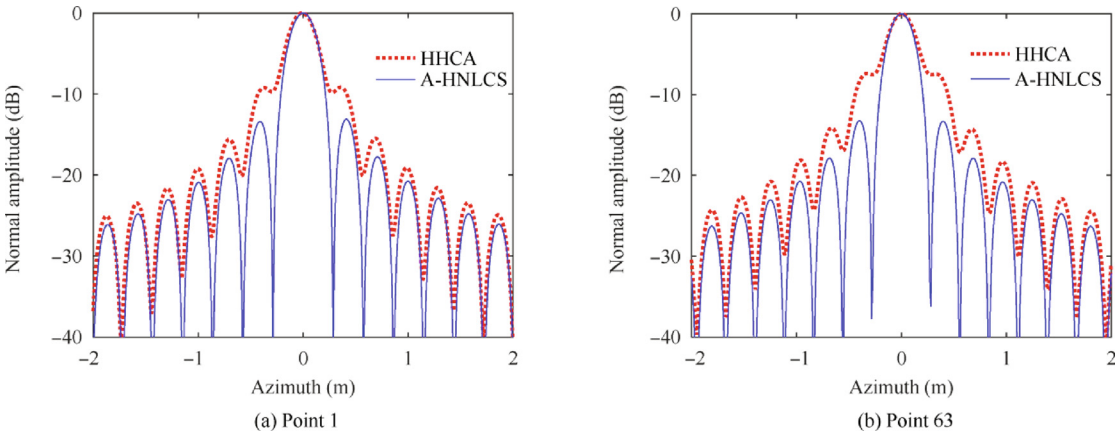

Fig. 11 Azimuth profiles of point 1 and point 63 for HHCA and A-HNLCS algorithm.

Table 3 Analysis of computational complexity for different algorithms.

Algorithm	AHRE	A-NLCS	HHCA	A-HNLCS
Times of range FT	4	4	4	4
Times of azimuth FT	3	3	3	3
Times of complex multiplications	5	4	8	9

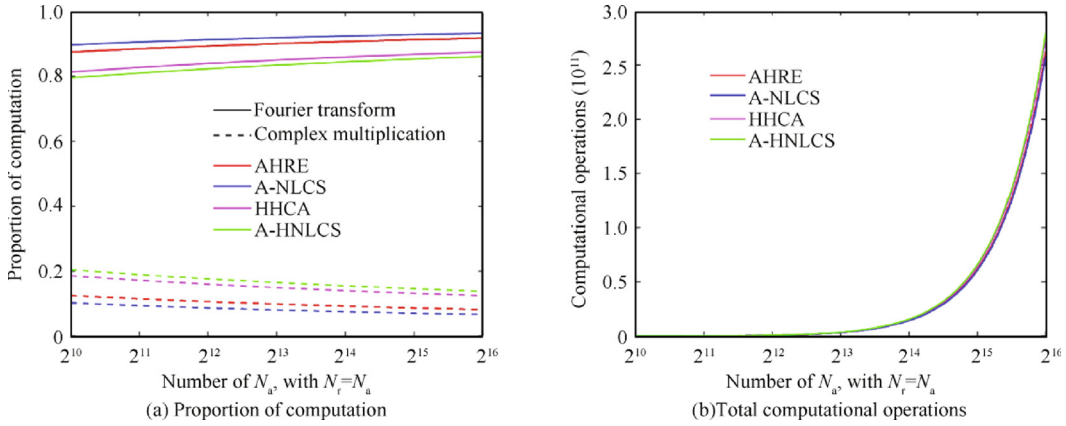

Fig. 12 Proportion of computation and total computational operations of four different algorithms for a range of N_a and N_r.

echo into several parts and stitching sub-images after processing. Hence, the increasing computational complexity of A-HNLCS is acceptable to some extent.

5. Conclusions

As a trend for future remote sensing technology, high-resolution wide-swath spaceborne SAR requires more precise range models and more effective imaging algorithms.

(1) Based on the analysis of azimuth-variance error in the range model, a second-order equivalent squint range model was developed to describe the range history for a larger azimuth swath.
(2) An advanced high-order nonlinear chirp scaling algorithm for HRWS spaceborne SAR was proposed, where sub-aperture processing was used to remove the azimuth variance and azimuth aliasing, the higher-order nonlinear chirp scaling algorithm was derived for accurate focusing, and the residual azimuth variance, imaging aliasing and geometric distortion were removed by a modified re-sampling operation.
(3) Simulation results have been provided to demonstrate the effectiveness of the proposed imaging algorithm. The proposed SOESRM and A-HNLCS algorithm can also be applied to other SAR systems where a larger azimuth swath is required.

Acknowledgement

This work was supported by the National Natural Science Foundation of China (No. 61861136008).

Appendix A. Approximate expression of SOERSM

Approximate expression Eq. (9) of SOERSM Eq. (7) is derived as following. The high order range model can be written as

$$R(t,r_0,x_0) = \sqrt{r_0^2 - 2r_0v_0\Delta t\cos\varphi_0 + \Delta a_2\Delta t^2 + \Delta a_3\Delta t^3 + \Delta a_4\Delta t^4} \tag{A1}$$

where $\Delta t = t - t_0$.

Based on the Taylor polynomial, Eq. (A1) can be expanded as

$$R(t,r_0,x_0) = r_0 + \frac{\partial R(t)}{\partial t}t + \frac{1}{2}\cdot\frac{\partial^2 R(t)}{\partial t^2}t^2 + \frac{1}{6}\cdot\frac{\partial^3 R(t)}{\partial t^3}t^3 + \frac{1}{24}\cdot\frac{\partial^4 R(t)}{\partial t^4}t^4 + \cdots \tag{A2}$$

with

$$\begin{cases} \frac{\partial R(t)}{\partial t} = -v_0\cos\varphi_0 \\ \frac{\partial^2 R(t)}{\partial t^2} = \frac{\Delta a_2 - v_0^2\cos^2\varphi_0}{r_0} \\ \frac{\partial^3 R(t)}{\partial t^3} = \frac{3\Delta a_3}{r_0} + \frac{3\Delta a_2 v_0\cos\varphi_0 - 3v_0^3\cos^3\varphi_0}{r_0^2} \\ \frac{\partial^4 R(t)}{\partial t^4} = \frac{12\Delta a_4}{r_0} + \frac{12\Delta a_3 v_0\cos\varphi_0}{r_0^2} - \\ \frac{3\Delta a_2^2 - 18\Delta a_2 v_0^2\cos^2\varphi_0 + 15v_0^4\cos^4\varphi_0}{r_0^3} \end{cases}$$

Then, Eq. (7) can be rewritten as

$$R(t,r_0,x_0) \approx r_0 - v_0\cos\varphi_0\Delta t + \tfrac{1}{2}\tfrac{\Delta a_2' - v_0^2\cos^2\varphi_0}{r_0}\Delta t^2 + \tfrac{1}{6}\left(\tfrac{3\Delta a_3'}{r_0} + \tfrac{3\Delta a_2' v_0\cos\varphi_0}{r_0^2} - \tfrac{3v_0^3\cos^3\varphi_0}{r_0^2}\right)\Delta t^3 + \tfrac{1}{24}\left(\tfrac{12\Delta a_4}{r_0} + \tfrac{12\Delta a_3' v_0\cos\varphi_0}{r_0^2} - \tfrac{3(\Delta a_2')^2 - 18\Delta a_2' v_0^2\cos^2\varphi_0 + 15v_0^4\cos^4\varphi_0}{r_0^3}\right)\Delta t^4 \tag{A3}$$

Substituting Eq. (8) to Eq. (A3), we have

$$\begin{aligned} R(t,r_0,x_0) &\approx r_0 - v_0\cos\varphi_0\Delta t + \frac{1}{2}\cdot\frac{v_0^2 - v_0^2\cos^2\varphi_0}{r_0}\Delta t^2 \\ &+ \frac{1}{6}\left[\frac{3\left(\Delta a_3 + \frac{\lambda r_0}{6}\xi_1(r_0)\right)}{r_0} + \frac{3v_0^3\cos\varphi_0}{r_0^2} - \frac{3v_0^3\cos^3\varphi_0}{r_0^2}\right]\Delta t^3 \\ &+ \frac{1}{24}\left[\frac{12\left(\Delta a_4 + \frac{\lambda r_0}{24}\xi_2(r_0)\right)}{r_0} + \frac{12\left(\Delta a_3 + \frac{\lambda r_0}{6}\xi_1(r_0)\right)v_0\cos\varphi_0}{r_0^2} - \frac{3v_0^4 - 18v_0^4\cos^2\varphi_0 + 15v_0^4\cos^4\varphi_0}{r_0^3}\right]\Delta t^4 \\ &- \frac{\lambda}{4}M\Delta t^2 - \left[\frac{\lambda}{12}(\xi_1(r_0) + \xi_2(r_0)t_0) + \frac{\lambda}{4r_0}Mv_0\cos\varphi_0\right]\Delta t^3 \\ &- \left[\frac{\lambda}{48}\xi_2(r_0) + \frac{\lambda}{12r_0}v_0\cos\varphi_0(\xi_1(r_0) + \xi_2(r_0)t_0) + \frac{\lambda^2}{32r_0}M^2 - \frac{\lambda v_0^2}{8r_0^2}M + \frac{3\lambda v_0^2\cos^2\varphi_0}{8r_0^2}M\right]\Delta t^4 \end{aligned} \tag{A4}$$

$$M = \xi_1(r_0)t_0 + \frac{1}{2}\xi_2(r_0)t_0^2$$

Since r_0 is much larger than other terms, Eq. (A4) can then be written as

$$\begin{aligned} R(t,r_0,x_0) &\approx R_1(t,r_0,x_0) - \tfrac{\lambda}{4}M\Delta t^2 - \tfrac{\lambda}{12}(\xi_1(r_0) + \xi_2(r_0)t_0)\Delta t^3 - \tfrac{\lambda}{48}\xi_2(r_0)\Delta t^4 \\ &= R_1(t,r_0,x_0) - \tfrac{\lambda}{4}M(t-t_0)^2 - \tfrac{\lambda}{12}(\xi_1(r_0) + \xi_2(r_0)t_0)(t-t_0)^3 - \tfrac{\lambda}{48}\xi_2(r_0)(t-t_0)^4 \end{aligned} \tag{A5}$$

By expanding Eq. (A5) and omitting the high order terms of $t_0^p t^q$, where $p > 0$ and $q > 1$, we have

$$\begin{aligned} R(t,r_0,x_0) &\approx R_1(t,r_0,x_0) - \tfrac{\lambda\xi_1(r_0)}{12}t^3 - \tfrac{\lambda\xi_2(r_0)}{48}t^4 + \left(\tfrac{\lambda\xi_1(r_0)t_0^2}{4} + \tfrac{\lambda\xi_2(r_0)t_0^3}{12}\right)\Delta t + \tfrac{\lambda\xi_1(r_0)t_0^3}{12} + \tfrac{\lambda\xi_2(r_0)t_0^4}{48} \\ &= R_1(t,r_0,x_0) + R_2(t,r_0,x_0) + R_3(t,r_0,x_0) \end{aligned} \tag{A6}$$

where

$$\begin{cases} R_1(t,r_0,x_0) = \sqrt{r_0^2 - 2r_0v_0\Delta t\cos\varphi_0 + v_0^2\Delta t^2 + \left(\Delta a_3 + \frac{\lambda r_0\xi_1(r_0)}{6}\right)\Delta t^3 + \left(\Delta a_4 + \frac{\lambda r_0\xi_2(r_0)}{24}\right)\Delta t^4} \\ R_2(t,r_0,x_0) = -\frac{\lambda\xi_1(r_0)}{12}t^3 - \frac{\lambda\xi_2(r_0)}{48}t^4 \\ R_3(t,r_0,x_0) = \left(\frac{\lambda\xi_1(r_0)t_0^2}{4} + \frac{\lambda\xi_2(r_0)t_0^3}{12}\right)\Delta t + \frac{\lambda\xi_1(r_0)t_0^3}{12} + \frac{\lambda\xi_2(r_0)t_0^4}{48} \end{cases} \tag{A7}$$

Appendix B. 2-D point target spectrum

2-D point target spectrum of the received signal are derived as following.

From Eq. (15), we have

$$S(f_a,f_\tau,r_0,x_0) = \sigma_0 W_r(f_\tau)W_a(f_a)\exp\left(-j\frac{\pi f_\tau^2}{K_r}\right) \cdot \exp\left(-j2\pi f_a t_a(f_a,f_\tau,r_0,x_0) - j4\pi\left(\frac{1}{\lambda} + \frac{f_\tau}{c}\right)R(t_a(f_a,f_\tau,r_0,x_0))\right) \tag{B1}$$

where f_a is the azimuth frequency, f_τ is the range frequency, $t_a(f_a,f_\tau,r_0,x_0)$ is the stationary point, obtained by solving the following equation:

$$2\left(\frac{1}{\lambda} + \frac{f_\tau}{c}\right)\frac{\partial R(t_a(f_a,f_\tau,r_0,x_0))}{\partial t} + f_a = 0 \tag{B2}$$

The MESRM Eq. (7) can be expanded into its Taylor series as

$$R(t,r_0) = r_0 - v_0t\cos\varphi_0 + \frac{v_0^2\sin^2\varphi_0}{2r_0}t^2 + \left(\frac{\Delta a_3'}{2r_0} + \frac{v_0^3\cos\varphi_0\sin^2\varphi_0}{2r_0^2}\right)t^3 + \left(\frac{\Delta a_4'}{2r_0} + \frac{\Delta a_3' v_0\cos\varphi_0}{2r_0^2} - \frac{v_0^4\sin^2\varphi_0\left(1-5\cos^2\varphi_0\right)}{8r_0^3}\right)t^4 + \cdots \tag{B3}$$

where $\Delta a_3' = \Delta a_3 + \frac{\lambda r_0\xi_1(r_0)}{6}$ and $\Delta a_4' = \Delta a_4 + \frac{\lambda r_0\xi_2(r_0)}{24}$.

Neglecting the first-order item $-v_0t\cos\varphi_0$ firstly, which would be reconsidered later, the range model can be written as

$$R_{\text{temp}}(t,r_0) = r_0 + K_2t^2 + K_3t^3 + K_4t^4 + \cdots \tag{B4}$$

where K_2, K_3 and K_4 represent parameters of the second-order, third-order and forth-order of t, respectively.

Using the series reversion[26] and substituting Eq. (B4) to Eq. (B3), the stationary point can be derived as

$$t_a = \alpha(Pf_a) + \beta(Pf_a)^2 + \gamma(Pf_a)^3 \tag{B5}$$

where

$$\begin{cases} \alpha = 1/(2K_2) \\ \beta = -3K_3/\left(8K_2^3\right) \\ \gamma = \left(9K_3^2 - 4K_2K_4\right)/\left(16K_2^5\right) \\ P = -c/[2(f_c + f_\tau)] \end{cases} \tag{B6}$$

The expression of the phase is

$$\begin{aligned} &\Phi_{\text{temp}}(f_a,f_\tau,r_0,x_0) = -j\frac{\pi f_\tau^2}{K_r} \\ &t - j\pi\left[2f_at_a + 4\left(\frac{1}{\lambda} + \frac{f_\tau}{c}\right)\left(r_0 + K_2t^2 + K_3t^3 + K_4t^4 + \cdots\right)\right] \\ &\quad = -j\frac{\pi f_\tau^2}{K_r} - j\pi\left[2\frac{1}{P}Pf_at_a - \frac{2}{P}\left(r_0 + K_2t^2 + K_3t^3 + K_4t^4 + \cdots\right)\right] \end{aligned} \tag{B7}$$

Substituting Eq. (B5) to Eq. (B7), we have

$$\Phi_{\text{temp}}(f_{\text{a}},f_{\tau},r_0,x_0)=-\text{j}\frac{\pi f_{\tau}^2}{K_{\text{r}}}-\text{j}\pi\left(-\frac{2r_0}{P}+\alpha P f_{\text{a}}^2+\frac{2}{3}\beta P^2 f_{\text{a}}^3+\frac{1}{2}\gamma P^3 f_{\text{a}}^4\right) \tag{B8}$$

By reconsidering the first-order item, the expression of received signal in time domain is

$$s(\tau,t,r_0,x_0)=s_{\text{temp}}\left(\tau-\frac{2K_1 t}{\text{c}},t,r_0,x_0\right)\exp\left(-\text{j}2\pi\frac{2f_{\text{c}}K_1}{\text{c}}t\right) \tag{B9}$$

Based on the theory of Fourier Transform, the 2-D point target spectrum of the received signal is

$$\begin{aligned}S(f_{\text{a}},f_{\tau},r_0,x_0)&=S\left(f_{\text{a}}+\frac{2K_1}{c}(f_{\tau}+f_{\text{c}}),f_{\tau},r_0,x_0\right)\\&=\sigma_0 W_{\text{r}}(f_{\tau})W_{\text{a}}\left(f_{\text{a}}+\frac{2K_1}{c}(f_{\tau}+f_{\text{c}})\right)\\&\quad\cdot\exp\left\{\Phi_{\text{temp}}\left(f_{\tau},f_{\text{a}}+\frac{2K_1}{c}(f_{\tau}+f_{\text{c}})\right)\right\}\end{aligned} \tag{B10}$$

Then

$$\Phi(f_{\text{a}},f_{\tau},r_0,x_0)=-\text{j}\frac{\pi f_{\tau}^2}{K_{\text{r}}}-\text{j}\pi\left(-\frac{2r_0}{P}+\frac{\alpha}{P}(Pf_{\text{a}}-K_1)^2+\frac{2\beta}{3P}(Pf_{\text{a}}-K_1)^3+\frac{\gamma}{2P}(Pf_{\text{a}}-K_1)^4\right) \tag{B11}$$

By substituting Eq. (B6) to Eq. (B11), we expand Eq. (B11) and obtain the following expression of the phase in frequency domain:

$$\begin{aligned}\Phi(f_{\text{a}},f_{\tau},r_0,x_0)=&-\text{j}\frac{\pi f_{\tau}^2}{K_{\text{r}}}-\text{j}\frac{4\pi}{\lambda}\left[r_0-\frac{\lambda^2(f_{\text{a}}-f_{\text{d}})^2}{8}\alpha+\frac{\lambda^3(f_{\text{a}}-f_{\text{d}})^3}{24}\beta-\frac{\lambda^4(f_{\text{a}}-f_{\text{d}})^4}{64}\gamma\right]\\&-\text{j}\frac{4\pi}{\text{c}}\left[r_0+\frac{\lambda^2(f_{\text{a}}^2-f_{\text{d}}^2)}{8}\alpha-\frac{\lambda^3(2f_{\text{a}}+f_{\text{d}})(f_{\text{a}}-f_{\text{d}})^2}{24}\beta+\frac{\lambda^4(3f_{\text{a}}+f_{\text{d}})(f_{\text{a}}-f_{\text{d}})^3}{64}\gamma\right]f_{\tau}\\&+\text{j}4\pi\left[\frac{\lambda f_{\text{a}}^2}{8f_{\text{c}}^2}\alpha-\frac{\lambda^2 f_{\text{a}}^2(f_{\text{a}}-f_{\text{d}})}{8f_{\text{c}}^2}\beta+\frac{3\lambda^3 f_{\text{a}}^2(f_{\text{a}}-f_{\text{d}})^2}{32f_{\text{c}}^2}\gamma\right]f_{\tau}^2\end{aligned} \tag{B12}$$

Based on the proposed SOESRM, the expression of the 2-D point target spectrum of the received signal can be derived as

$$\begin{aligned}&S(f_{\text{a}},f_{\tau},r_0,x_0)\\&=\sigma_0 W_{\text{r}}(f_{\tau})W_{\text{a}}(f_{\text{a}})\exp\left(-\text{j}2\pi f_{\text{a}}t_{\text{a}}(f_{\text{a}},f_{\tau},r_0,x_0)-\text{j}4\pi\left(\frac{1}{\lambda}+\frac{f_{\tau}}{c}\right)R(t_{\text{a}}(f_{\text{a}},f_{\tau},r_0,x_0))\right)\\&\approx\sigma_0 W_{\text{r}}(f_{\tau})W_{\text{a}}(f_{\text{a}})\exp(\Phi_{\text{azi}}(f_{\text{a}},r_0,x_0))\exp(\Phi_{\text{HOP}}(f_{\text{a}},f_{\tau},r_0,x_0))\\&\cdot\exp(\Phi_{\text{RCM}}(f_{\text{a}},f_{\tau},r_0,x_0))\exp(\Phi_{\text{rg2}}(f_{\text{a}},f_{\tau},r_0,x_0))\\&\cdot\exp\left\{-\text{j}\pi\frac{4\xi_1(r_{\text{ref}})t_0^3+\xi_2(r_{\text{ref}})t_0^4}{12}\right\}\exp\left\{\text{j}\pi\frac{(f_{\text{a}}-f_{\text{d}}')^2\Delta\xi_1(r_0)t_0}{f_{\text{r}}^2}\right\}\end{aligned} \tag{B13}$$

where

$$\Phi_{\text{azi}}(f_{\text{a}},r_0,x_0)=-\text{j}\frac{4\pi}{\lambda}\left[r_0'-\frac{\lambda^2(f_{\text{a}}-f_{\text{d}}')^2}{8}\alpha(r_0)+\frac{\lambda^3(f_{\text{a}}-f_{\text{d}}')^3}{24}\beta(r_0)-\frac{\lambda^4(f_{\text{a}}-f_{\text{d}}')^4}{64}\gamma(r_0)\right] \tag{B14}$$

$$\begin{aligned}\Phi_{\text{RCM}}(f_{\tau},f_{\text{a}},r_0,x_0)=&-\text{j}\frac{\pi}{c}\left[4r_0'+\frac{\lambda^2(f_{\text{a}}^2-f_{\text{d}}^2)}{2}\alpha(r_0)-\frac{\lambda^3(2f_{\text{a}}+f_{\text{d}}')(f_{\text{a}}-f_{\text{d}}')^2}{6}\beta(r_0)\right]f_{\tau}\\&-\text{j}\frac{\pi\lambda^4(3f_{\text{a}}+f_{\text{d}}')(f_{\text{a}}-f_{\text{d}}')^3}{64c}\gamma(r_0)f_{\tau}\end{aligned} \tag{B15}$$

$$\Phi_{\text{rg2}}(f_{\tau},f_{\text{a}},r_0,x_0)=-\text{j}\frac{\pi f_{\tau}^2}{K_{\text{r}}}+\text{j}\frac{\pi\lambda f_{\text{a}}^2}{2f_{\text{c}}^2}\left[\alpha(r_0)-\lambda(f_{\text{a}}-f_{\text{d}}')\beta(r_0)+\frac{3\lambda^2(f_{\text{a}}-f_{\text{d}}')^2}{4}\gamma(r_0)\right]f_{\tau}^2 \tag{B16}$$

$$\begin{aligned}\Phi_{\text{HOP}}(f_{\tau},f_{\text{a}},r_0,x_0)=&-\text{j}2\pi f_{\text{a}}t_{\text{a}}(f_{\tau},f_{\text{a}},r_0,x_0)-\text{j}4\pi\left(\frac{1}{\lambda}+\frac{f_{\tau}}{c}\right)R(t_{\text{a}}(f_{\tau},f_{\text{a}},r_0,x_0))\\&-\Phi_{\text{azi}}(f_{\text{a}},r_0,x_0)-\Phi_{\text{RCM}}(f_{\text{a}},f_{\tau},r_0,x_0)-\Phi_{\text{rg2}}(f_{\text{a}},f_{\tau},r_0,x_0)\end{aligned} \tag{B17}$$

where $t_a(\cdot)$ is the stationary point, $r_0'=r_0+\frac{\lambda\xi_1(r_0)}{12}t_0^3+\frac{\lambda\xi_2(r_0)}{48}t_0^4$, $f_{\text{d}}'(r_0,x_0)=f_{\text{d}}(r_0,0)+\Delta f_{\text{d}}(r_0,x_0)$, $\Delta\xi_1(r_0)=\xi_1(r_0)-\xi_1(r_{\text{ref}})$. $f_{\text{d}}',f_{\text{d}},f_{\tau},f_{\text{r3}}$ and f_{r4} represent $f_{\text{d}}'(r_0,x_0),f_{\text{d}}(r_0,0),f_{\tau}(r_0,0),f_{\text{r3}}(r_0,0)$ and $f_{\text{r4}}(r_0,0)$, respectively. α,β and γ are the Doppler parameters of the echo signal. They can be calculated as $\alpha=\frac{-2}{\lambda f_{\text{r}}(r_0)}$, $\beta=\frac{-2f_{\text{r3}}(r_0)}{\lambda^2 f_{\text{r}}^3(r_0)}$ and $\gamma=\frac{4f_{\text{r}}(r_0)f_{\text{r4}}(r_0)-12f_{\text{r3}}(r_0)}{3\lambda^3 f_{\text{r}}^5(r_0)}$.

References

1. Townsend W. An initial assessment of the performance achieved by the Seasat-1 radar altimeter. *IEEE J Oceanic Eng* 1980;**5**(2):80–92.
2. Moreira A, Prats-Iraola P, Younis M, Krieger G, Hajnsek I, Papathanassiou KP. A tutorial on synthetic aperture radar. *IEEE Geosci Remote Sens Mag* 2013;**1**(1):6–43.
3. Morena LC, James KV, Beck J. An introduction to the RADARSAT-2 mission. *Can J Remote Sens* 2004;**30**(3):221–34.
4. Buckreuss S, Balzer W, Muhlbauer P, et al. The TerraSAR-X satellite project. *Proceedings of the 2003 IEEE International Geoscience and Remote Sensing Symposium*. Toulouse, France. Piscataway: IEEE Press; 2005.
5. Werninghaus R, Buckreuss S. The TerraSAR-X Mission and System Design. *IEEE Trans Geosci Remote Sens* 2010;**48**(2):606–14.
6. Krieger G, Moreira A, Fiedler H, Hajnsek I, Werner M, Younis M, Zink M. TanDEM-X: A Satellite Formation for High-Resolution SAR Interferometry. *IEEE Trans Geosci Remote Sens* 2007;**45**(11):3317–41.
7. Covello F, Battazza F, Coletta A, Lopinto E, Fiorentino C, Pietranera L, Valentini G, Zoffoli S. COSMO-SkyMed an existing opportunity for observing the Earth. *J Geodyn* 2010;**49**(3-4):171–80.
8. Arikawa Y, Saruwatari H, Hatooka Y, et al. ALOS-2 launch and early orbit operation result. *Proceedings of the 2014 IEEE International Geoscience and Remote Sensing Symposium*. Quebec City, Canada. Piscataway: IEEE Press; 2014.
9. Calabrese D, Germani C, Torre A, et al. CSG status and new solutions to increase the product portfolio. *Proceedings of the 12th European conference on synthetic aperture radar EUSAR*. Aachen, Germany. Berlin: VDE; 2018.
10. Janoth J, Gantert S, Koppe W, et al. TerraSAR-X2 – mission overview. *Proceedings of the 2012 IEEE international geoscience and remote sensing symposium*. Munich, Germany. Piscataway: IEEE Press; 2012.
11. Juergen J, Markus J, Lutz P, et al. High resolution wide swath – the next generation X-band mission. *Proceedings of the 2019 IEEE international geoscience and remote sensing symposium*. Yokohama, Japan. Piscataway: IEEE Press; 2019.
12. Men ZR, Wang PB, Li CS, et al. High-temporal-resolution high-spatial-resolution spaceborne SAR based on continuously varying PRF. *Sensors* 2017;**17**(8):1700.
13. Mittermayer J, Moreira A, Loffeld O. Spotlight SAR data processing using the frequency scaling algorithm. *IEEE Trans Geosci Remote Sens* 1999;**37**(5):2198–214.
14. Sun XB, Yeo TS, Zhang CB, et al. Time-varying step-transform algorithm for high squint SAR imaging. *IEEE Trans Geosci Remote Sens* 1999;**37**(6):2668–77.
15. Luo Y, Zhao B, Han X, et al. A novel high-order range model and imaging approach for high-resolution LEO SAR. *IEEE Trans Geosci Remote Sens* 2014;**52**(6):3473–85.

16. Huang L, Qiu X, Hu D, Ding C. Focusing of Medium-Earth-Orbit SAR With Advanced Nonlinear Chirp Scaling Algorithm. *IEEE Trans Geosci Remote Sens* 2011;**49**(1):500–8.
17. Wang P, Liu W, Chen J, Niu Mu, Yang W. A High-Order Imaging Algorithm for High-Resolution Spaceborne SAR Based on a Modified Equivalent Squint Range Model. *IEEE Trans Geosci Remote Sens* 2015;**53**(3):1225–35.
18. Meng TT, Tan GW, Li MH, et al. Chirp Scaling algorithm based on Chebyshev orthogonal decomposition for curve trajectory SAR. *Acta Aeronaut Astronaut Sinica* 2020;**41**(8) [Chinese].
19. Raney RK, Runge H, Bamler R, et al. Precision SAR processing using chirp scaling. *IEEE Trans Geosci Remote Sens* 1994;**32**(4):786–99.
20. Wang P, Liu W, Chen J, Yang W, Han Yu. Higher order nonlinear chirp scaling algorithm for medium Earth orbit synthetic aperture radar. *J Appl Remote Sens* 2015;**9**(1):096084.
21. Felipe Queiroz DA, Marwan Y, Gerhard K, et al. A new slow PRI variation scheme for multichannel SAR high-resolution wide-swath imaging. *Proceedings of the 2018 IEEE international geoscience and remote sensing symposium*. Valencia, Spain. Piscataway: IEEE Press; 2018.
22. Queiroz de Almeida F, Younis M, Krieger G, Moreira A. Multichannel Staggered SAR Azimuth Processing. *IEEE Trans Geosci Remote Sens* 2018;**56**(5):2772–88.
23. Yoon YT, Eineder M, Yague-Martinez N, Montenbruck O. TerraSAR-X Precise Trajectory Estimation and Quality Assessment. *IEEE Trans Geosci Remote Sens* 2009;**47**(6):1859–68.
24. Ding C, Liu J, Lei B, et al. Preliminary exploration of systematic geolocation accuracy of GF-3 SAR satellite system. *J Radars* 2017;**6**(1):11–6 [Chinese].
25. Zhou XK, Chen J, Wang PB, et al. An efficient imaging algorithm for GNSS-R bi-static SAR. *Remote Sens* 2019;**11**(24):2945.
26. Dwight HB. *Tables of integrals and other mathematical data*. New York: The MacMillan Company; 1947. p. 11–2.

Please cite this article in press as: MEN Z et al. Advanced high-order nonlinear chirp scaling algorithm for high-resolution wide-swath spaceborne SAR, *Chin J Aeronaut* (2020), https://doi.org/10.1016/j.cja.2020.08.035